

## Supplementary Information for Energy and Excitation Loss Accounting in UV-absorbing Organic Photovoltaics with Efficient Charge Transfer Exciton Emission

Quinn C. Burlingame,<sup>1,\*†</sup> Xiao Liu,<sup>2,\*</sup> Melissa L. Ball,<sup>1</sup> Barry P. Rand,<sup>1,2</sup> and Yueh-Lin Loo<sup>3,†</sup>

\* Q.C.B. and X.L. contributed equally to this work

<sup>1</sup> Andlinger Center for Energy and the Environment, Princeton University, Princeton, NJ, USA

<sup>2</sup> Department of Electrical and Computer Engineering, Princeton University, Princeton, NJ, USA

<sup>3</sup> Department of Chemical and Biological Engineering, Princeton, NJ, USA

† Correspondence: qb@princeton.edu, lloo@princeton.edu

### Table of Contents

<b>Methods</b> .....	2
<b>Supplemental Note 1</b> .....	5
<b>Figure S1</b> .....	6
<b>Figure S2</b> .....	7
<b>Figure S3</b> .....	8
<b>Figure S4</b> .....	9
<b>Figure S5</b> .....	10
<b>Figure S6</b> .....	11
<b>Figure S7</b> .....	12
<b>Figure S8</b> .....	13
<b>Figure S9</b> .....	14
<b>Figure S10</b> .....	15
<b>Figure S11</b> .....	16
<b>Figure S12</b> .....	17
<b>Figure S13</b> .....	18
<b>Supplemental References</b> .....	19

## Methods

**Materials:** The organic materials N,N'-bis(9,9-dimethyl-9H-fluoren-2-yl)-N,N'-diphenylbenzidine (BF-DPB), 4,6-bis[3,5-(dipyrid-4-yl)phenyl]-2-methylpyrimidine (B4PymPm), 1,3,5-tris(n-phenylbenzimidazol-2-yl)benzene (TPBi), bathophenanthroline (BPhen), and 1,3,4,5,7,8-hexafluorotetracyanonaphthoquinodimethane (F6-TCNNQ) were purchased from Luminescence Technology Corp. and were used as received. Aluminum (99.999% purity) was purchased from Kurt J. Lesker Co., while Li (99% purity) and MoO<sub>3</sub> (99.97% purity) were purchased from MilliporeSigma. All metals and metal oxides were used as received. The organic donor molecules BF-DPP, BF-DPT, BF-DPN, and BF-DPA were synthesized and purified *via* sublimation as described previously.<sup>1</sup> Pre-patterned indium tin oxide (ITO)-coated substrates were purchased from Luminescence Technology Corp.

**Film and device fabrication:** Organic thin films were deposited and OPV devices were fabricated in a thermal evaporator at rates of 0.05 to 2 Å/s under vacuum < 5×10<sup>-7</sup> Torr. Thicknesses and deposition rates were monitored using quartz crystal microbalances. Prior to deposition, quartz slides (for thin film characterization) and ITO-coated glass substrates (for OPV devices) were sequentially sonicated in deionized water, acetone, and isopropanol before drying in a stream of N<sub>2</sub> gas. Device substrates were then cleaned in a UV-ozone chamber for 10 min. Non-transparent OPVs with all five donors employed the structure in **Fig. 3a**, while the fully transparent OPVs used for *in operando* transient absorption measurements employed the structure shown in **Fig. S11k**. The indium tin oxide (ITO) layer on top of the structure in **Fig. S11k** was deposited *via* radio frequency sputtering of a 3" diameter 90/10 wt.% InO<sub>3</sub>/SnO<sub>3</sub> sputtering target at 45 W to produce a growth rate of 0.22 Å/s. The process pressure was 3 mTorr with a 15 sccm Ar flow supplied as the sputtering gas. The OPVs were placed as far as possible from the sputtering target during ITO deposition to avoid damage (~ 25 cm), but most were still partially shunted or fully short-circuited. To recover OPV performance, a reverse bias of -20 V was applied to each device for ~30 s to eliminate any shunt paths.<sup>1-3</sup>

**Photovoltaic characterization:** The external quantum efficiency (EQE) of each OPV

was calculated *via* 
$$EQE(\lambda) = \frac{hc}{q\lambda} R_{ref}(\lambda) \frac{I_{OPV}(\lambda)}{I_{ref}(\lambda)}$$
, where  $h$  is Planck's constant,  $c$  is the speed of light,  $q$  is the charge of an electron,  $\lambda$  is the wavelength,  $R_{ref}(\lambda)$  is the calibrated responsivity of a Si photodiode,  $I_{OPV}(\lambda)$  is the wavelength-dependent photocurrent measured with a lock-in amplifier on each OPV in response to monochromatic, fiber-coupled, chopped (200 Hz) light, and  $I_{ref}(\lambda)$

is the photocurrent measured in the same way on the calibrated Si reference photodiode. Current density vs. voltage ( $J$ - $V$ ) characteristics of the OPVs were measured under illumination from a Xe arc lamp solar simulator using a current-voltage sourcemeter. To calibrate the incoming light intensity and correct for spectral mismatch between the solar simulator and the AM1.5G spectrum, the  $EQE$  of the OPVs was integrated over the solar spectrum to produce an integrated 1-sun short-circuit current. The intensity of the light source was then set to produce this amount of photocurrent in each illuminated OPV operating at 0 V.

***Photoluminescence, transient photoluminescence, photoluminescence quantum yield, and electroluminescence:*** Steady-state and transient photoluminescence of organic thin films were measured using an Edinburgh Instruments FLS980 fluorescence spectrometer, where samples were excited by a Xenon arc lamp followed by a monochromator and a pulsed laser at the wavelength of 375nm, respectively. The measurement and calculation of photoluminescence quantum yield (PLQY) follows the methods described elsewhere.<sup>4</sup> A 404 nm laser was directed into the integrating sphere to excite the film. All spectra were collected using a fiber-coupled monochromator (SpectraPro HRS-300) equipped with a Si charge-coupled device array (PIXIS:400).

***Voltage-dependent photocurrent, photoluminescence, and electroluminescence:*** A 404 nm diode laser with a pump power of  $\sim 10 \mu\text{W}$  was passed through a linear polarizer, then chopped at 200 Hz before it was focused onto the OPV. Emission from the OPV was then passed through a 2<sup>nd</sup> linear polarizer with a  $90^\circ$  polarization angle to block as much of the reflected/scattered pump beam as possible. A 450 nm long-pass filter was also employed to block the pump beam. Emission from the OPV was collected using a spectrometer and was averaged over several cycles. To electrically bias the OPV, a low-noise DC power supply was placed in series/parallel with an OPV in series with a transimpedance amplifier. To avoid any inaccuracy associated with the voltage drop across the amplifier, a high precision sourcemeter was used to measure the voltage across the OPV. The photocurrent was transformed into a voltage by the transimpedance amplifier with a gain of  $1 \text{ V}/10 \mu\text{A}$ , and its magnitude was recorded by a lock-in amplifier. Electroluminescence from the OPVs was collected using the same setup with the excitation laser off and with a positive voltage bias from the sourcemeter.

***Transient absorption and voltage-dependent transient absorption:*** For the transient absorption measurements within the time window of 0-7 ns, a 1 kHz regeneratively amplified Ti:Sapphire laser (Coherent Libra) with a commercial optical parametric amplifier (OPerA Solo)

and commercial transient absorption spectrometer (Ultrafast Systems Helios) were used. The output pulse of the Ti:Sapphire laser, centered at 800 nm with a duration of  $\sim 45$  fs and pulse power of 4 W, was split with a 90/10 (reflection/transmission) beamsplitter to generate the pump and probe. The reflected portion was directed into the OPerA to generate the pump at  $\lambda = 380$  nm. The pump pulse was chopped at 500 Hz with its polarization controlled by a broadband  $\lambda/2$  waveplate and then attenuated to 60  $\mu$ W (a pulse fluence of 30  $\mu$ J/cm<sup>2</sup>) before being focused into the sample position. The transmitted portion, i.e. the probe, was mechanically delayed and then focused into a sapphire crystal to generate a white light continuum from 410 nm to 860 nm with its intensity and polarization controlled by a combination of the  $\lambda/2$  waveplate and polarizer. The probe beam passed through the same sample position as the pump, and entered a CCD camera for detection. All experiments on this setup were done at the “magic angle”<sup>5</sup> to avoid reorientation effects of the samples on the nanosecond timescale. For the transient absorption measurement at the  $\mu$ s-timescale, the pump was generated using the same methods described above, while the probe was generated using a commercial photonic crystal fiber (Ultrafast Systems EOS) which operates at 1kHz and was electronically delayed with respect to the pump pulse to realize a time window of up to 2400 $\mu$ s. A constant excitation power, i.e. power per pulse, was kept across experiments. Because the photoactive materials are organic, with low dielectric constants  $<4$ , all are expected to be polaronic. This is consistent with the broad absorption band observed in some heterojunction blends, for example, in **Fig. S9c**.

**Global fitting of transient absorption spectrograms:** Global fitting was performed using an open-source fitting program, Glotaran.<sup>6</sup> Prior to fitting, all spectra were chirp corrected and their background signal prior to time zero was subtracted. A sequential model with three components was employed to fit the Frenkel to CT and CT to polaron transitions, yielding the corresponding time constants.

**Density functional theory calculations:** Time-dependent density functional theory performed by Schrodinger software version 2021-2.<sup>7</sup> The charge transfer energies and orbitals used B3LYP/LACVP\* for the analysis and employed the Material Science suite from Schrodinger. Triplet energy calculations used B3LYP-D3 and 6-31++G\*\*.

## Supplemental Note 1: Derivation of rate equations

For singlet excitons:

$$G = [S_1](k_{CT} + k_S) \quad (1)$$

For singlet CTEs:

$$[S_1]k_{CT} + \frac{1}{4}\gamma[CS]^2 = [{}^1CTE](k_{r,S-CT} + k_{nr,S-CT} + k_{diss}(V)) \quad (2)$$

For triplet CTEs:

$$\frac{3}{4}\gamma[CS]^2 = [{}^3CTE](k_{nr,T-CT} + k_{diss}(V) + k_T) \quad (3)$$

For monomolecular triplets:

$$[T_1]k_{nr,T} = [{}^3CTE]k_T \quad (4)$$

and finally for charge separated states (i.e. polarons):

$$([{}^3CTE] + [{}^1CTE])k_{diss}(V) = \gamma[CS]^2 + [CS]k_{SRH} + J_{photo}(V)/q \quad (5)$$

Since only CTE emission is observed from HJs and the rate of donor singlet decay ( $\tau_S$  in **Table 3**) is more than 3 orders of magnitude slower than the rate of charge transfer ( $\tau_{CT}$  in **Table 3**), Eq. 1 can be reduced by assuming that  $[S_1]k_S$  is negligibly small, thus:

$$G = [S_1]k_{CT} \quad (6)$$

Eq. 6 can be plugged into Eq. 2, yielding:

$$G + \frac{1}{4}\gamma[CS]^2 = [{}^1CTE](k_{r,S-CT} + k_{nr,S-CT} + k_{diss}(V)) \quad (7)$$

Eq. 4 can be plugged into Eq. 3, yielding:

$$\frac{3}{4}\gamma[CS]^2 = [{}^3CTE](k_{nr,T-CT} + k_{diss}(V)) + [T_1]k_{nr,T} \quad (8)$$

and Eq. 7 and Eq. 8 can be summed as follows:

$$G + \gamma[CS]^2 = [{}^1CTE](k_{r,S-CT} + k_{nr,S-CT} + k_{diss}(V)) + [{}^3CTE](k_{nr,T-CT} + k_{diss}(V)) + [T_1]k_{nr,T} \quad (9)$$

Subtracting Eq. 5 from Eq. 9 yields a unified equation which accounts for all excitation sources and sinks in the OPV:

$$G = [{}^1CTE](k_{r,S-CT} + k_{nr,S-CT}) + [{}^3CTE]k_{nr,T-CT} + [T_1]k_{nr,T} + [CS]k_{SRH} + J_{photo}(V)/q \quad (10)$$

Dividing through by  $G$  yields the fraction of excitations that are dissipated by each of the

recombination and extraction mechanisms:

$$1 = \frac{[{}^1CTE]k_{r,S-CT}}{G} + \frac{[{}^1CTE]k_{nr,S-CT}}{G} + \frac{[{}^3CTE]k_{nr,T-CT}}{G} + \frac{[T_1]k_{nr,T}}{G} + \frac{[CS]k_{SRH}}{G} + \frac{J_{photo}(V)/q}{G} \quad (11)$$

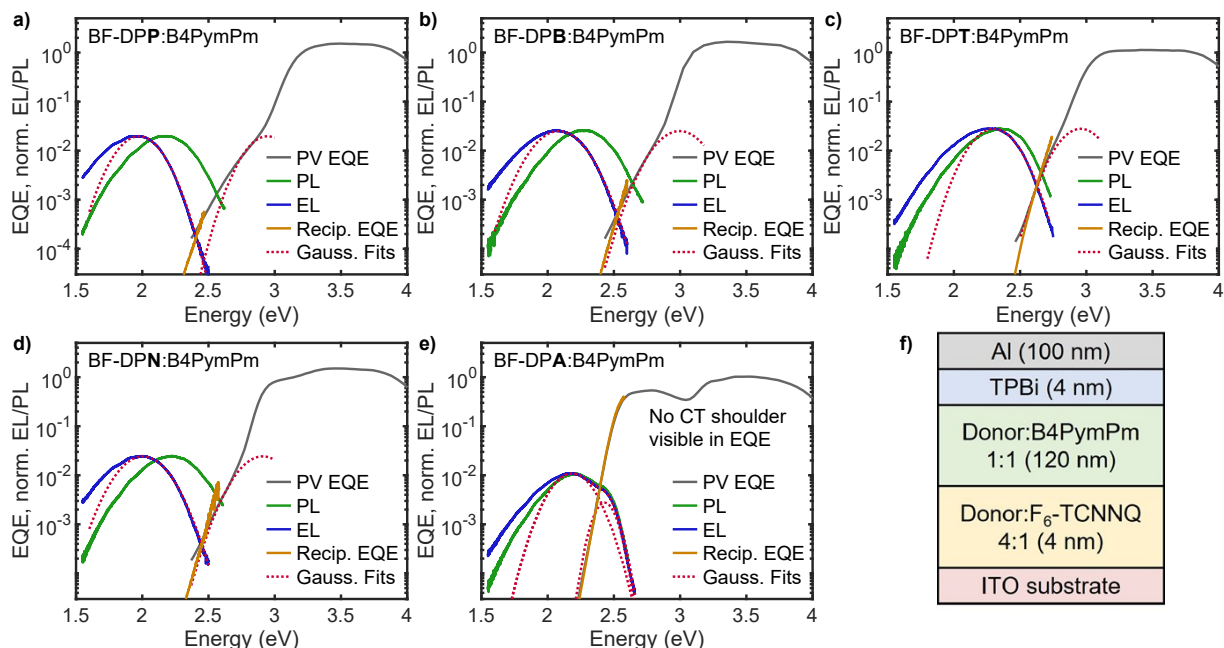


**Figure S1 | Quantum efficiency, emission spectra, and device structures. a-e)** Reduced photovoltaic EQE spectra ( $\text{EQE} \times E$ ) and normalized reduced PL ( $\text{PL}/E$ ) and electroluminescence ( $\text{EL}/E$ ) spectra for devices with the structure shown in **f** and the donor indicated in each panel. The PV EQE calculated from the reciprocity relationship between EQE and EL is shown as the orange lines in **a-e**:  $\text{EQE}_{\text{recip}}(E) \propto I_{\text{EL}}(E) / I_{\text{BB}}(E)$ , where  $I_{\text{EL}}(E)$  and  $I_{\text{BB}}(E)$  are the EL and blackbody spectra at room temperature. Gaussian fits to the reduced EL and PV EQE are shown as red dotted lines on each spectrum. The CTE shoulder is not visible in the spectrum collected on the OPV with BF-DPA (**e**), as it is obscured by singlet absorption. A shoulder is visible, however, in its EL/PL spectra.

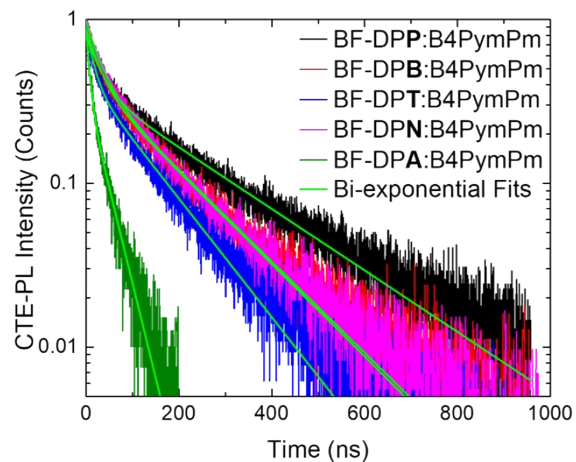


**Figure S2 | Transient photoluminescence spectra.** Transient PL spectra collected on 80nm blended HJ films with bi-exponential fits shown. The amplitude-averaged lifetimes for each are given in **Table 1**.

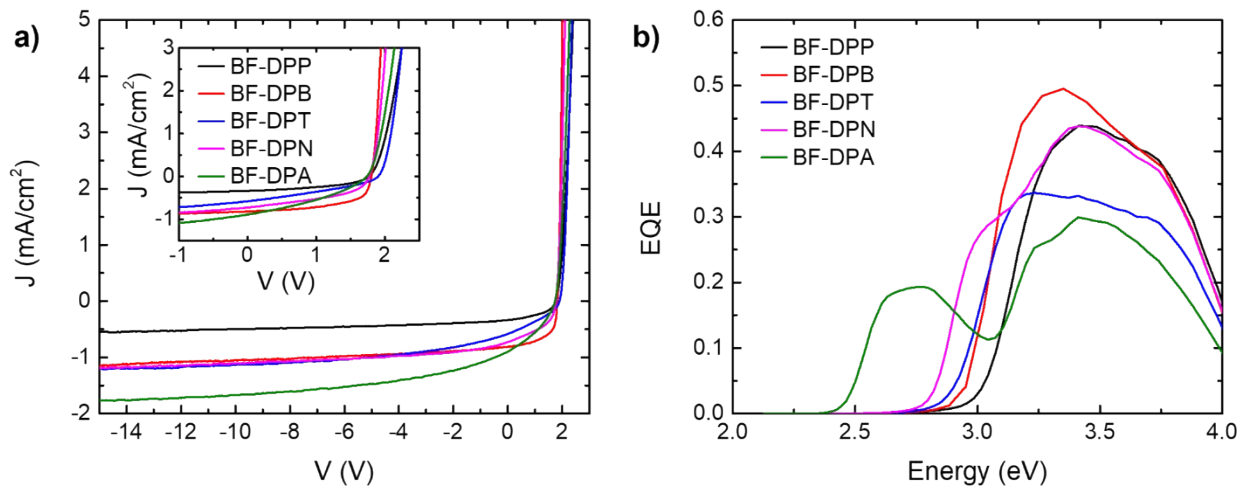


**Figure S3 | Photovoltaic device characterization.** **a)** Current density vs. voltage curves for 120 nm HJ devices with the structure in **Fig. 3f** measured out to -15V reverse bias. The inset shows a zoomed view highlighting the IV<sup>th</sup> quadrant, which is most relevant for photovoltaic performance. **b)** EQE spectra for the same devices.

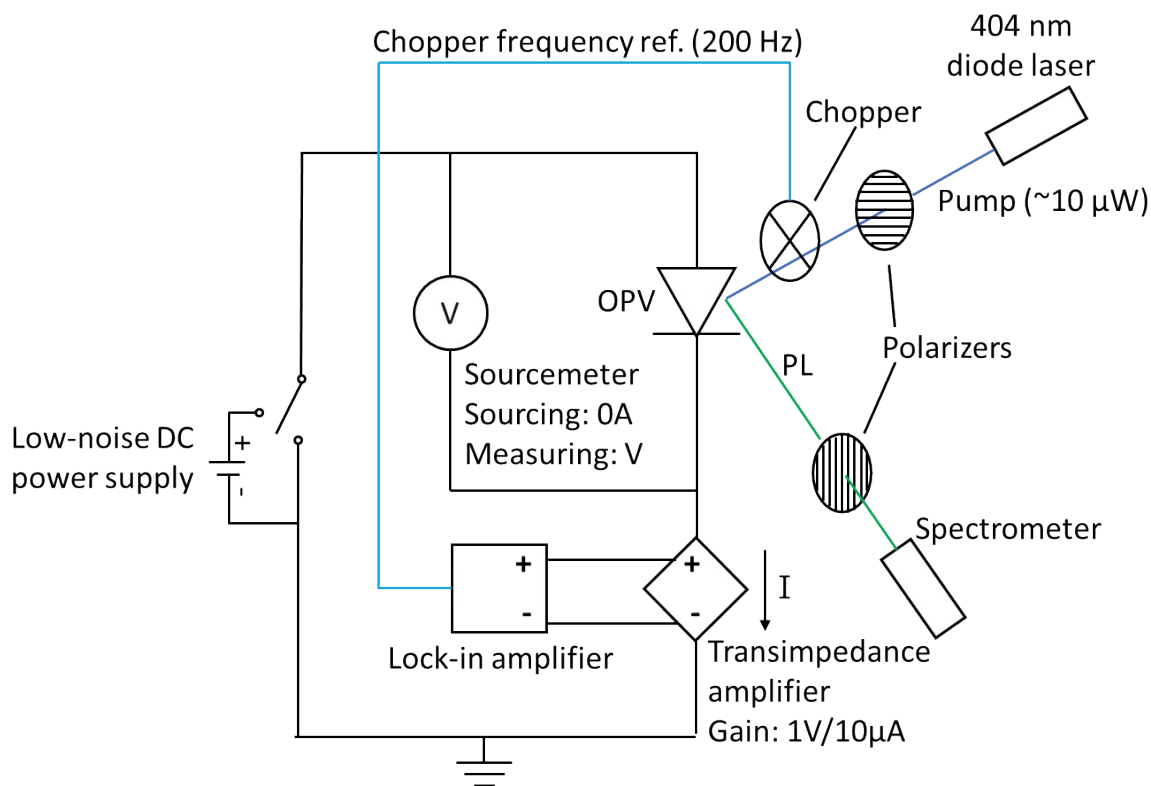


**Figure S4 | Voltage-dependent photocurrent and photoluminescence measurement setup.** A depiction of the optical setup and electrical circuit used to simultaneously measure voltage-dependent photocurrent and PL spectra. The operation of this system is described in **Methods**.

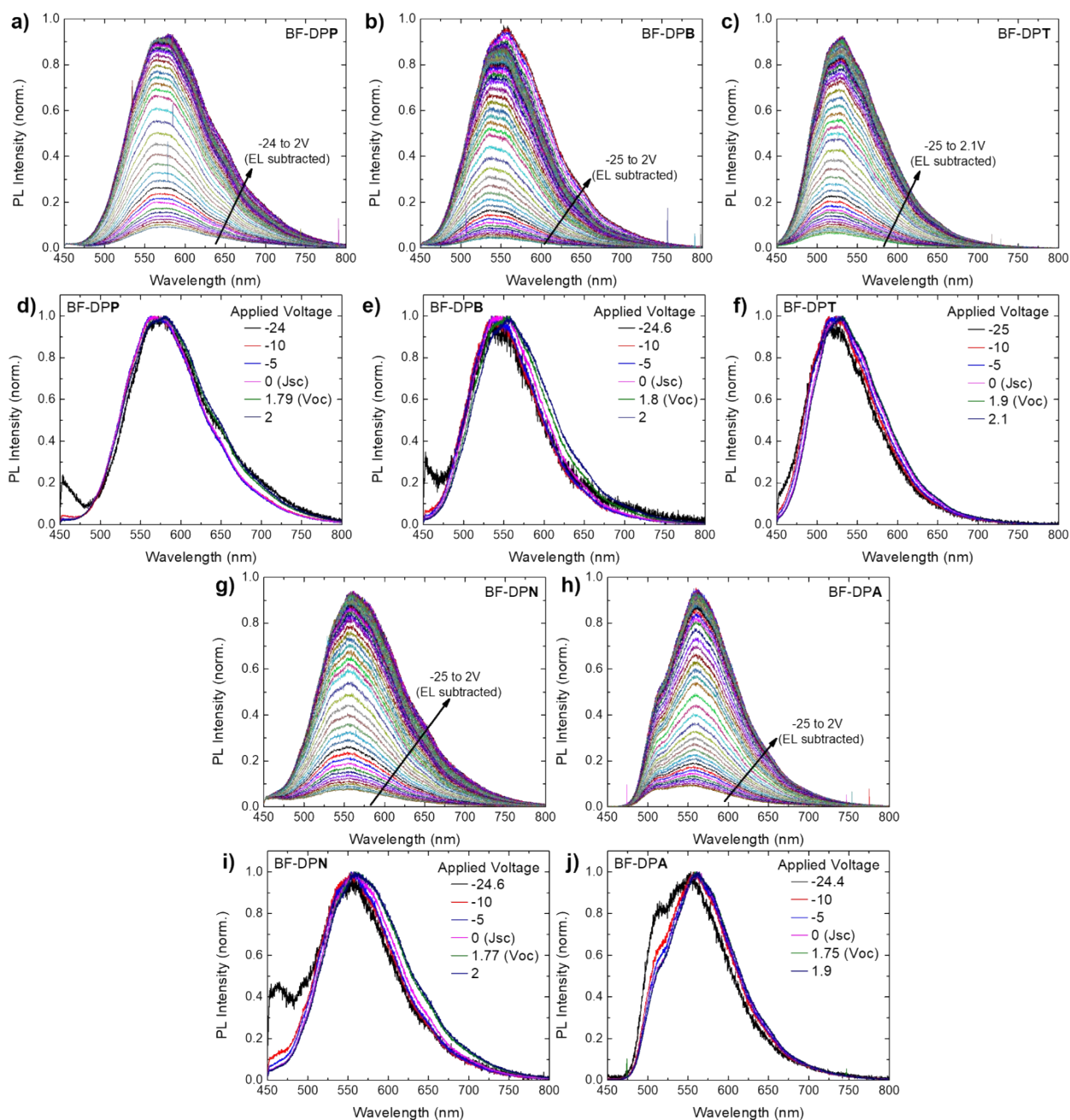


**Figure S5 | Voltage-dependent photoluminescence spectra. a-c and g,h)**

Photoluminescence spectra collected as a function of voltage using the setup shown in **Fig. S4** and described in **Methods**. Since a weak EL signal begins to appear in the PL spectra at voltages approaching  $V_{OC}$  and deeper into forward bias, an EL only spectrum was collected without the pump beam at each forward bias condition which was then subtracted from the PL to get the signals shown. Panels **d-f** and **i,j** show the intensity-normalized PL spectra at several different bias conditions to show how the energy of the PL emission changes with voltage. Since the pump beam has a consistent intensity that appears as a 2<sup>nd</sup> feature in the spectra at 450-500 nm, it appears to grow in the normalized spectra with increasing reverse bias as the intensity of the CTE emission decreases.

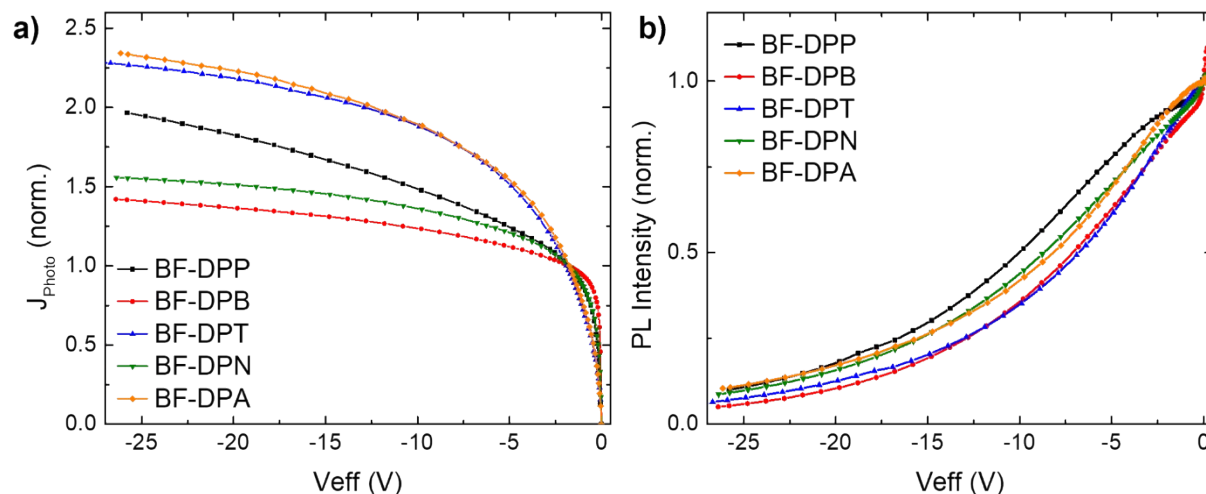


**Figure S6 | Voltage-dependent photocurrent and integrated PL intensity. a)** Voltage-dependent photocurrent collected from OPVs using the setup shown in **Fig. S4** and described in **Methods**. The effective voltage ( $V_{\text{eff}}$ ) is defined as the applied voltage minus  $V_{\text{OC}}$ . All photocurrents were normalized by  $J_{\text{SC}}$  for comparison. **b)** Voltage-dependent PL intensity integrated across the spectra in **Fig. S5a,b,c,g and h**. Each was normalized by its value at  $V_{\text{OC}}$  ( $V_{\text{eff}} = 0$ ).

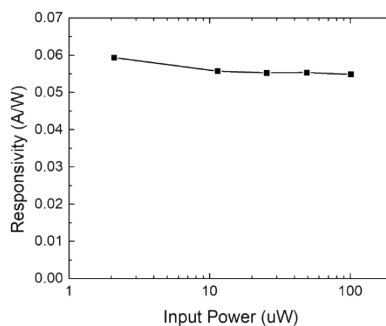


**Figure S7 | Intensity dependence of large reverse bias photocurrent.** To ensure that the photocurrents observed at reverse bias were a result of direct optical excitation of the organic photoactive layer, rather than a photo-modulated injection current (i.e., due to increased conductivity or barrier lowering), a BF-DPA:B4PymPm OPV was held at a constant bias of -15 V and the intensity of the 408 nm pump laser was varied by one order of magnitude above and below the test condition ( $\sim 10 \mu\text{W}$ ) while its photocurrent was measured. The responsivity (photocurrent/incident power) of the OPV is nearly flat, indicating that the observed current is indeed photocurrent.

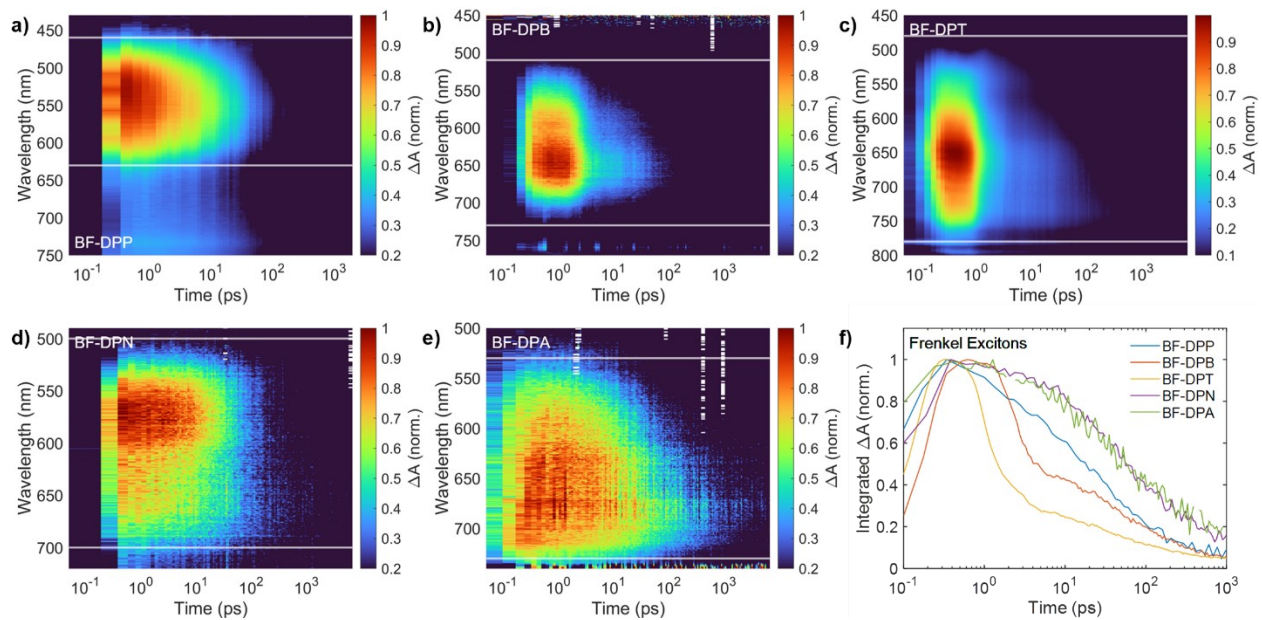


**Figure S8 | Transient absorption spectra on neat films. a-e)** Transient absorption spectra of neat films of the five donors. The horizontal white lines on each plot indicate the region of the spectrum that was integrated to produce the transients shown in panel f.

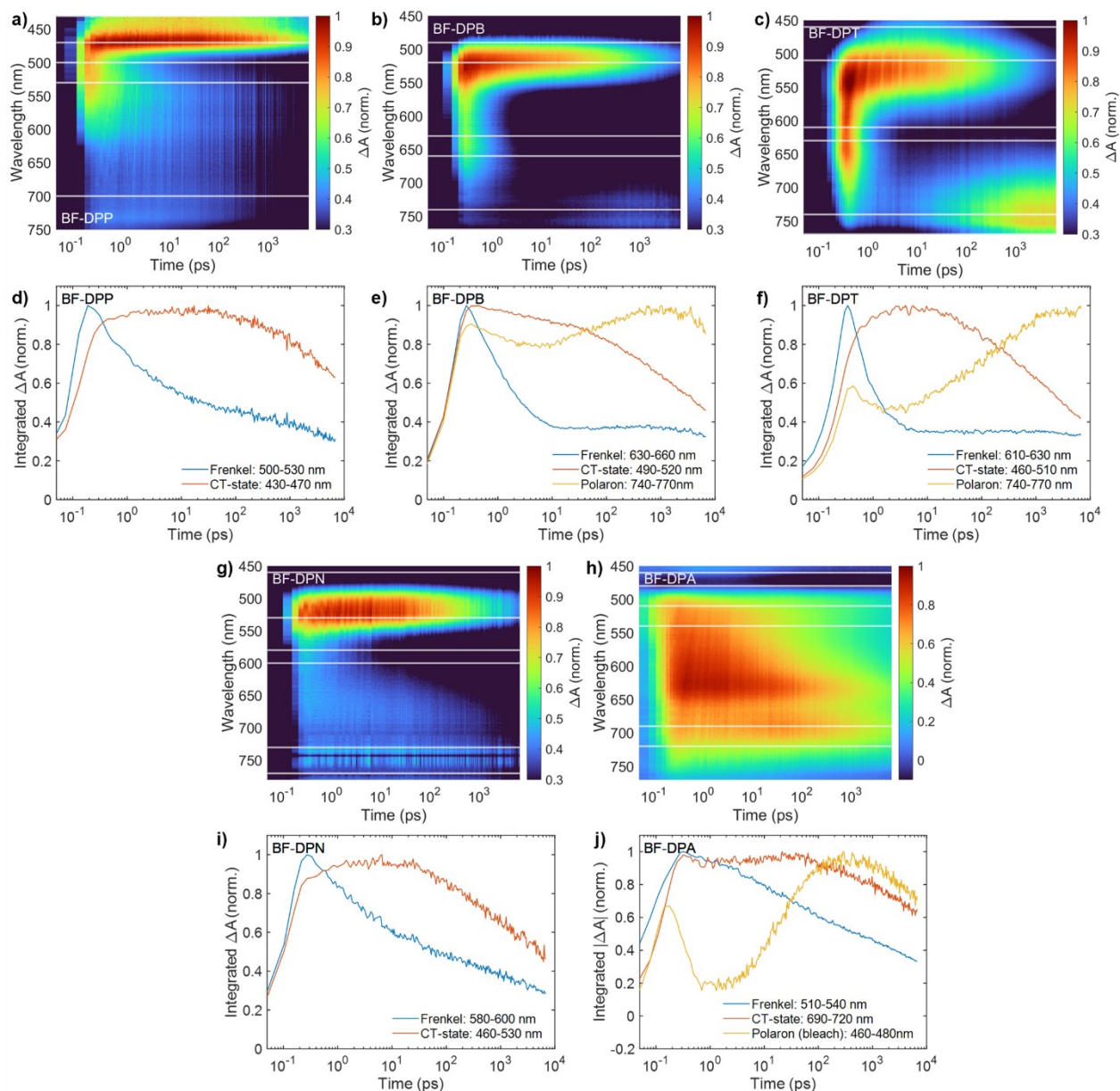


**Figure S9 | Transient absorption spectra on blended films < 6 ns.** a-c and g,h) Transient absorption spectra of 120 nm donor:B4PymPm bulk HJ films. The horizontal white lines indicate the integration ranges corresponding to Frenkel excitons, CTE states, and polarons. These integration ranges are also stated in the legends in panels d-f, i and j, which show the integrated changes in absorption across the stated wavelength bands. No polaron signal was observed in the BF-DPP:B4PymPm or BF-DPN:B4PymPm spectra, presumably because it is outside the spectral range of the measurement. The BF-DPA:B4PymPm spectrum (h) has a high energy bleach from 460 – 480 nm, which we attribute to polaron formation, and thus plot the absolute value of the absorption change to view the dynamics of this polaron bleach with those of the Frenkel and CTE state. The slight rise visible in the Frenkel exciton transients in panels e and f at  $t > 10$  ps results from the formation of polarons, which also absorb weakly in the Frenkel integration range employed for BF-DPB:B4PymPm and BF-DPT:B4PymPm.

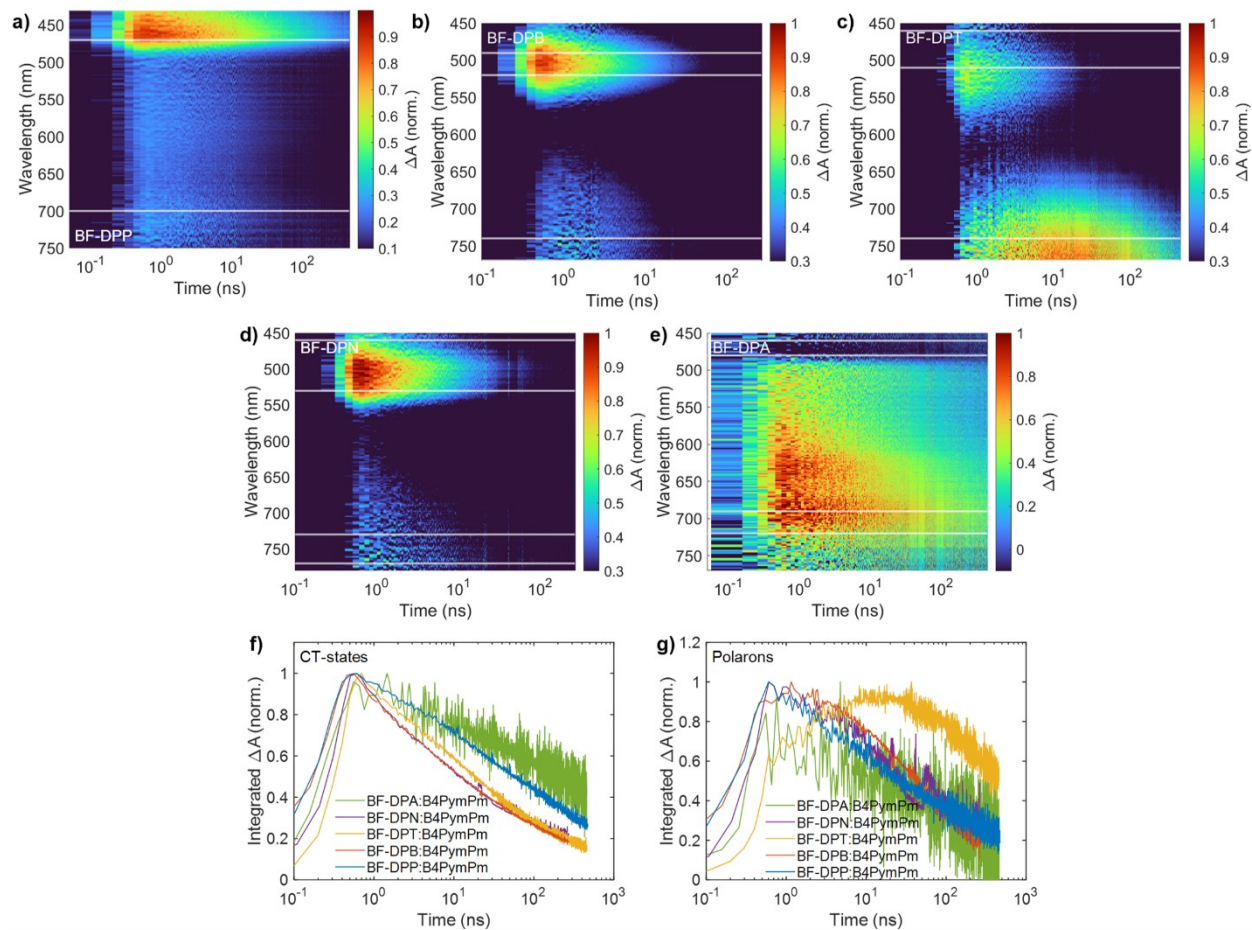


**Figure S10 | Transient absorption spectra on blended films < 500 ns.** a-e) Transient absorption spectra of 120 nm donor:B4PymPm bulk HJ films measured over 500 ns. The horizontal white lines indicate the integration ranges corresponding to CTE states and polarons. f,g) Integrated transients of the five films corresponding to CTE states (f) and polarons (g).

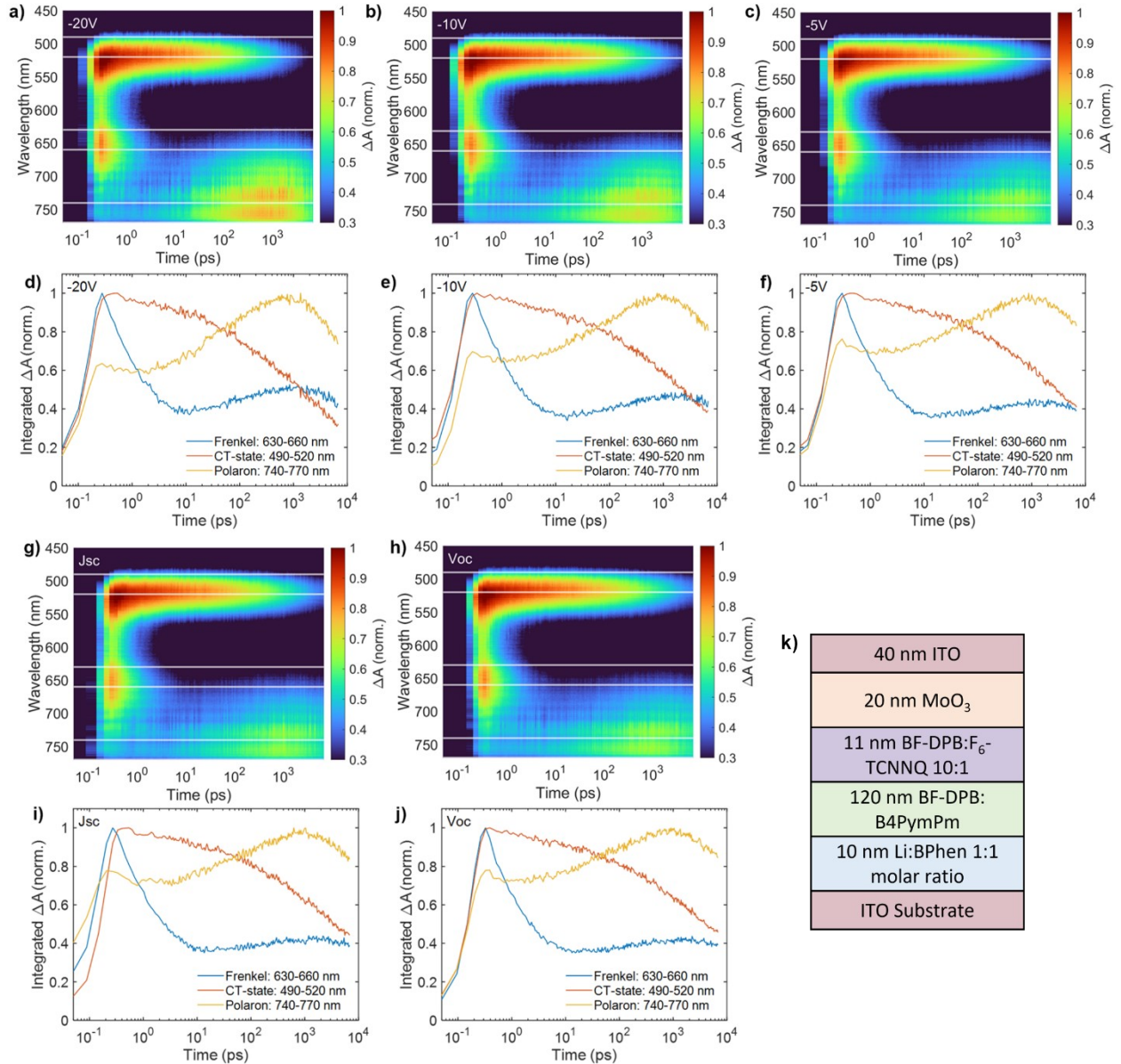


**Figure S11 | Transient absorption spectra on full-stack OPVs as a function of voltage. a-c and g,h)** Transient absorption spectra on transparent BF-DPB:B4PymPm OPVs with the structure shown in **k** at five different bias conditions: -20 V, -10 V, -5 V, 0 V ( $J_{SC}$ ), and 1.8 V ( $V_{OC}$ ). The horizontal white lines indicate the integration ranges corresponding to Frenkel excitons, CTE states, and polarons. These integration ranges are also stated in the legends in panels **d,e,f,i** and **j**, which show the integrated changes in absorption across the stated wavelength bands. The compiled transients corresponding to Frenkel excitons, CTE states, and polarons are shown in **Fig. 6**. The slight rise in the Frenkel signal at times  $> 10$  ps results from the formation of polarons that also weakly absorb  $\sim 660$  nm light.

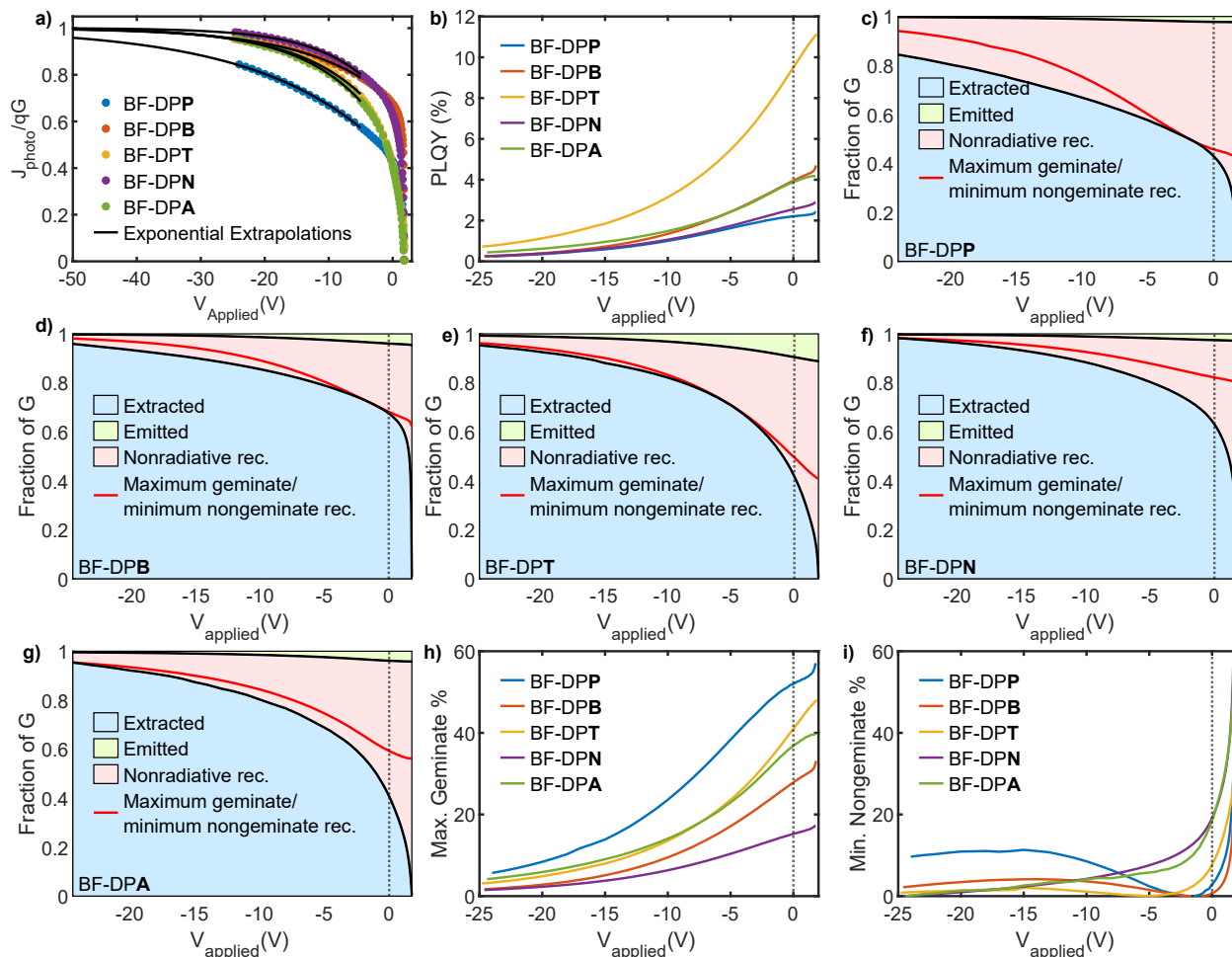


**Figure S12 | Voltage-dependent excitation fate analysis.** **a)** Voltage-dependent photocurrent of OPVs with all five donors normalized to the value of their exponentially extrapolated asymptote. Exponential extrapolations are shown as black lines. **b)** Voltage-dependent PLQY estimated by multiplying the zero-field PLQY in **Table 1** by the  $V_{OC}$ -normalized voltage-dependent PL values for each OPV. **c-g)** The voltage-dependent fraction of excitations that are extracted (blue shaded area), emitted (green shaded area), or recombine nonradiatively (red shaded area) for OPVs with each donor. The red lines represent the maximum amount of geminate and minimum amount of nongeminate recombination that could be present in the OPV. See **Analysis** for details. The voltage-dependent maximum percentage of recombination that could be occurring geminately in each OPV, and the minimum that could be occurring nongeminately are plotted separately in panels **h** and **i**.

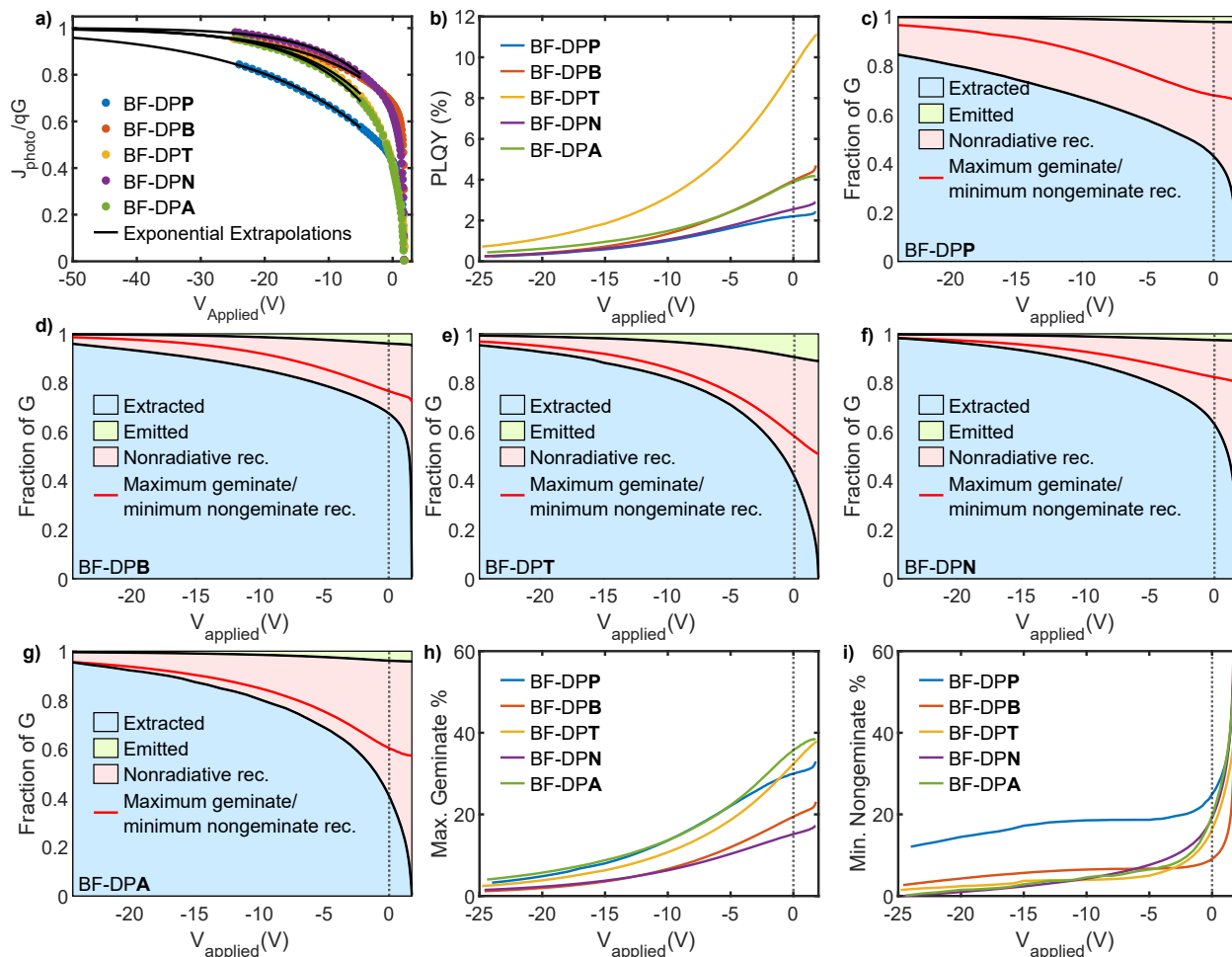


**Figure S13 | Voltage-dependent excitation fate analysis with the maximum geminate / minimum nongeminate fractions calculated subject to a monotonicity constraint. a)** Voltage-dependent photocurrent of OPVs with all five donors normalized to the value of their exponentially extrapolated asymptote. Exponential extrapolations are shown as black lines. **b)** Voltage-dependent PLQY estimated by multiplying the zero-field PLQY in **Table 3** by the  $V_{OC}$ -normalized voltage-dependent PL values for each OPV. **c-g)** The voltage-dependent fraction of excitations that are extracted (blue shaded area), emitted (green shaded area), or recombine nonradiatively (red shaded area) for OPVs with each donor. The red lines represent the maximum amount of geminate and minimum amount of nongeminate recombination that could be present in the OPV while keeping both fractions monotonic with voltage. See **Analysis** for details. The voltage-dependent maximum percentage of recombination that could be occurring geminately in each OPV, and the minimum that could be occurring nongeminately as calculated subject to this monotonicity constraint are plotted separately in panels **h** and **i**.

## Supplemental References

- 1 M. L. Ball, Q. Burlingame, H. L. Smith, T. Liu, S. R. Parkin, A. Kahn and Y.-L. Loo, *ACS Energy Lett*, 2022, **7**, 180–188.
- 2 P. E. Burrows, V. Bulovic, S. R. Forrest, L. S. Sapochak, D. M. McCarty and M. E. Thompson, *Appl Phys Lett*, 1994, **65**, 2922–2924.
- 3 L. M. Andersson, *Energy Technology*, 2015, **3**, 437–442.
- 4 F. Fries and S. Reineke, *Sci Rep*, 2019, **9**, 15638.
- 5 M. Bydder, A. Rahal, G. D. Fullerton and G. M. Bydder, *Journal of Magnetic Resonance Imaging*, 2007, **25**, 290–300.
- 6 J. J. Snellenburg, S. P. Liptonok, R. Seger, K. M. Mullen and I. H. M. van Stokkum, *J Stat Softw*, 2012, **49**, 1–22.
- 7 A. D. Bochevarov, E. Harder, T. F. Hughes, J. R. Greenwood, D. A. Braden, D. M. Philipp, D. Rinaldo, M. D. Halls, J. Zhang and R. A. Friesner, *Int J Quantum Chem*, 2013, **113**, 2110–2142.